Materials and Design 80 (2015) 28–35

Contents lists available at ScienceDirect

Materials and Design

journal homepage: www.elsevier.com/locate/matdes

Effect of directional solidification and porosity upon the superelasticity of Cu–Al–Ni shape-memory alloys

Bin Yuan [a,b,c,*], Peiqi Zheng [b], Yan Gao [a,c], Min Zhu [a,c], David C. Dunand [b]

[a] School of Materials Science & Engineering, South China University of Technology, Guangzhou 510640, China
[b] Department of Materials Science & Engineering, Northwestern University, Evanston, IL 60208, USA
[c] Key Laboratory of Advanced Energy Storage Materials of Guangdong Province, Guangzhou 510640, China

ARTICLE INFO

Article history:
Received 29 October 2014
Revised 11 April 2015
Accepted 2 May 2015
Available online 4 May 2015

Keywords:
High-temperature shape-memory alloy
Cu–Al–Ni alloy
Superelasticity
Porous
Stress-induced transformation

ABSTRACT

Strain incompatibilities between grains in polycrystalline Cu–Al–Ni shape-memory alloys undergoing stress-induced reversible transformation reduce their ductility and their recoverable superelastic strains on unloading. These strain incompatibilities can be mitigated by creation of large, textured grains through directional solidification or large, bamboo grains intersecting the free surfaces of pores. To study these two approaches to improve superelasticity in Cu–Al–Ni alloys, polycrystalline Cu–13.5Al–4Ni (wt.%) samples were cast in porous and dense form, with and without directional solidification. When tested in compression, directionally-solidified, oligocrystalline bulk (non-porous) Cu–Al–Ni exhibits recoverable unloading strains as high as 6.6% at 210 °C, as compared to 3.1% for their conventionally-solidified counterparts. Similarly, when comparing conventionally-solidified Cu–Al–Ni SMA with 58% open porosity shows 1.4% recoverable unloading strain at 260 °C, whereas a value of 2.6% is achieved in directionally-solidified porous samples with bamboo grains straddling pores. This improvement in superelasticity remains present after 30 mechanical load–unload cycles at 260 °C. Thus, both directional solidification and addition of porosity can reduce strain incompatibilities between neighboring grains in polycrystalline Cu–Al–Ni alloys, allowing them to approach the intrinsic high superelasticity of single crystals.

1. Introduction

Porous shape-memory alloys (SMAs) exhibit a combination of properties inherited from shape-memory alloys and porous metals, such as the shape-memory effect and superelasticity [1,2], low density [3], adjustable mechanical properties such as stiffness and strength [4], high specific surface area and good damping performance [5]. Thus, porous SMAs have many potential applications for bone replacement [6], energy absorber and electrode materials [7] and actuators [8]. Most studies have focused on porous NiTi, because this alloy shows stable shape memory and superelasticity in polycrystalline form, good biocompatibility and attractive mechanical properties (strength and stiffness) [1,9–11]. NiTi is however limited to relatively low transformation temperatures (usually <100 °C) [4], and is costly, due to the high cost of elements and the difficulty in casting the alloy with the required tight composition tolerances; the processing challenges are compounded for porous NiTi, which is, with rare exceptions [5], produced by powder-metallurgy [12]. By contrast, Cu-based SMAs are attractive because of their lower material and processing costs (in part due to their lower melting temperatures) and their higher transformation temperature [2,13].

There are two main Cu-based binary alloy systems with SMA capabilities: Cu–Zn and Cu–Al. Of the two, Cu–Al exhibits higher transformation temperatures and better microstructural stability. To prevent the decomposition of the parent phase in Cu–Al SMAs, nickel is usually added to form ternary Cu–Al–Ni SMAs [14]. Although the shape memory effect and mechanical properties of Cu–Al–Ni SMAs are inferior to those of NiTi SMAs in polycrystalline form, monocrystalline Cu–Al–Ni SMAs exhibit excellent superelasticity. For example, Cu–14%Al–4.2%Ni (wt.%) [001] single crystals show fully recoverable elastic/superelastic strains as high as 17% at 205 °C [15]. By contrast, polycrystalline Cu–Al–Ni SMAs exhibits very low superelasticity and ductility due to transgranular fracture caused by stress concentration at grain boundaries, especially at triple junctions [14]. Because of the high cost in producing monocrystalline alloys, various approaches have been taken to impart moderate ductility to polycrystalline Cu–Al–Ni SMAs. The

* Corresponding author at: School of Materials Science and Engineering, South China University of Technology, Guangzhou 510640, China.
E-mail address: apsheng@scut.edu.cn (B. Yuan).

http://dx.doi.org/10.1016/j.matdes.2015.05.001
0261-3069/

most effective method is to greatly reduce grain size by adding small amount of Ti, B and V [16,17], or to form crystallographic texture by rolling [18]. For example, Morris [19] found a maximum of 4.5% recoverable tensile strain for a $CuAl_{12}Ni_4Mn_4B_{0.04}$ alloy deformed to 5% total strain at 150 °C.

Recently, Chen et al. [20] reported that Cu–Al–Ni microwires with bamboo grain structure can show recoverable tensile strains as high as 6.8% at 50 °C. This was attributed to the low number of grain boundaries per unit volume and lack of triple junctions, so that the martensitic transformation stresses can be relieved at the free surfaces of the wire. Bertolino et al. [2] also reported that Cu–Zn–Al foams with 60–75% porosity, fabricated by liquid metal infiltration of a leachable bed of silica gel, exhibit up to ~4% superelastic strain recovery in compression at room temperature. However, to the authors' knowledge, porous SMAs with superelasticity at high temperature (>200 °C) have never been reported, and their mechanical cycle stability at high temperature is also unknown. In this study, we fabricated bulk (dense) and porous Cu–Al–Ni specimens with bamboo grain structure by directional solidification, and investigated their superelasticity at high temperature (>200 °C).

2. Materials and methods

Pure copper, aluminum and nickel (purity >99.9%) were arc-melted to obtain parent ingots with nominal composition of Cu–13.5Al–4Ni (wt.%). From these ingots, porous Cu–Al–Ni samples (diameter ~20 mm, height ~25 mm) were fabricated by liquid metal infiltration and replication with sodium aluminate as space-holder, a high-melting, chemically-stable, leachable oxide [2,21]. Within an alumina crucible, ~5 g of $NaAlO_2$ particles (355–510 μm size) were hand-packed into a loose preform over which a Cu–Al–Ni ingot was introduced. The loaded crucible was placed in a vertical vacuum tube furnace which was evacuated to 5×10^{-3} Pa residual pressure, heated to 1200 °C for 0.5 h so as to melt the alloy (and lightly sinter the $NaAlO_2$ preform), and then pressurized with Ar gas at 1.6 atm for 2 h to allow molten Cu–Al–Ni to infiltrate the preform of space-holder particles. After infiltration, some of specimens were solidified in the furnace (denoted as FC, for furnace-cooling) which was slowly and uniformly cooled by switching off its electrical power, while other specimens were directionally-solidified by withdrawing the tube from the furnace at a speed of 5 mm/min (denoted DS, for directional solidification), resulting in Cu–Al–Ni/$NaAlO_2$ composites. The $NaAlO_2$ interconnected phase was then removed from the composites by sonicating in 10% HCl for 20 h. Control Cu–Al–Ni bulk samples were fabricated by FC or DS, using the same procedures, except for the lack of space-holder. Unless noted specifically, all specimens described in the following were subsequently heat-treated to obtain the shape-memory effect by homogenizing at 900 °C for 30 min. in a tube furnace under flowing Ar and then quenching into ice water.

Polished cross-sections were observed by optical microscopy to assess grain size and pores, the latter being further studied with a Hitachi scanning electronic microscope (SEM) S-3400N. An Oxford EDS instrument attached to the SEM was used to determine the matrix composition of the porous Cu–Al–Ni alloys, calibrated with a Cu–Al–Ni standard sample whose chemical composition had been measured independently by wet chemical analysis.

The materials thermal properties were measured on small cut specimens using a Perkin Elmer DSC-7 differential scanning calorimeter (DSC) heated and cooled at a rate of 10 K/min. Phase transformations were determined in the DSC curve from the intersection between the baseline and the steepest slopes of the peak. From all ingots, cylindrical samples with 6 mm diameter and 12 mm height were cut by electro-discharge machining, and these samples were tested in uniaxial compression in a MTS Sintech 20/G testing system with a high temperature chamber in air, calculating strain from the cross-head displacement, after correction of the compliance of the testing system. All porous samples used for compression testing had porosities of 58 ± 3%, as determined by measurement of their volume and mass.

3. Results and discussion

3.1. Pore and grain microstructure

Fig. 1 illustrates the pore morphology of porous Cu–Al–Ni alloys before and after removing the $NaAlO_2$ space-holder phase. This figure shows that the molten alloy readily infiltrated the voids of the $NaAlO_2$ preform under the moderate gas pressure used here. To make the compressive results of porous Cu–Al–Ni samples comparable, all porous samples showed a narrow range of porosity (58 ± 3%) which was achieved by etching the porous samples in the same acid after the complete removal of the space-holder. It is apparent from Fig. 1b that pore size is ~300–550 μm, and these pores are interconnected and roughly equiaxed, which is consistent with the size and shape of $NaAlO_2$ particles.

Optical micrographs of FC and DS bulk sample are shown in Fig. 2a–b. The FC sample (Fig. 2a) exhibits coarse grains with size of ~1–1.5 mm, which are equiaxed, as determined from longitudinal cross-sections. By contrast, the DS sample shows non-equiaxed grains. In the transverse direction, the grains are polygonal with average size ~2–2.5 mm (Fig. 2b). In the longitudinal direction, the grains are elongated along the solidification direction with sizes reaching ~6 mm. Martensite plates can be clearly observed in all grains, indicating that the heat treatment achieved austenite phase, and that the martensitic transformation finish temperature (M_f) is above room temperature.

Fig. 3a–c shows optical micrographs of polished, etched cross-sections of FC and DS porous samples. Pores are surrounded by thin metal walls connected by thicker nodes. As for the bulk samples, martensite plates are present in all grains. In the FC porous samples (Fig. 3a), bamboo grains spanning entire wall sections can be observed (the white coarse arrows in Fig. 3a show grain boundaries), but multiple grains exist at the nodes (the white fine arrows in Fig. 3a show a triple point). By contrast, the DS porous sample shows only bamboo grains either in transverse or in longitudinal cross-section, as illustrated in Fig. 3b and c, even in walls wider than 1 mm. Moreover, fewer grain boundaries are observed as compared to the FC porous sample, indicating coarser grain size.

In all Cu–Al–Ni porous samples, all pores are interconnected and open to the surface because they were formed by dissolution of the pre-sintered $NaAlO_2$ space-holder, as also observed in Ni–Mn–Ga magnetic shape-memory foams fabricated by a similar process [21–23]. Because of their high porosity of ~58% and the sub-millimeter size of their space-holder, the porous Cu–Al–Ni samples exhibit walls that are typically below ~200 μm in thickness, as shown in Figs. 1b and 3a–c. The Cu–Al–Ni bulk samples have grain much larger for the DS case (~2 × 2 × 6 mm) than for the FC case (~1 × 1 × 1 mm), as shown in Fig. 2. These grains are also much larger than the thickness of most walls in the samples, indicating that bamboo grains spanning the width and even the length of the walls of the porous samples can easily be achieved by this simple processing method. This is confirmed by the microstructures shown in Fig. 3, where the DS foam exhibits larger grain size (~4–5 mm) than the FC porous sample (~1–1.5 mm). Thus, bamboo grains can be formed in the DS foam (Fig. 3b and C), whereas some grain boundary triple points can still be observed in the FC porous sample (Fig. 3a) although most walls and many nodes have bamboo grain structure.

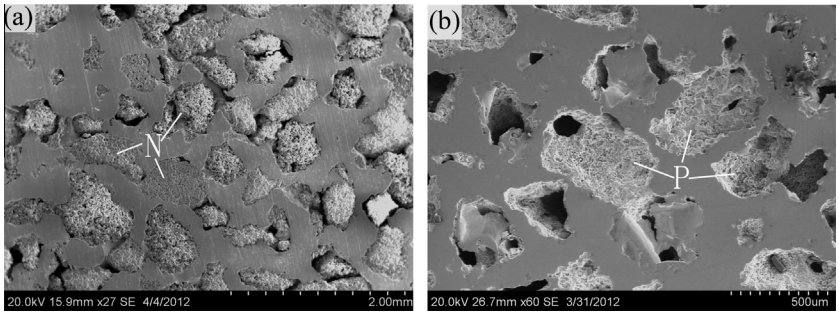

Fig. 1. SEM micrographs of cross-sections of DS foams: (a) before removal of $NaAlO_2$ space-holder (labeled N); (b) after removal of space-holder to form pores (labeled P), shown at higher magnification.

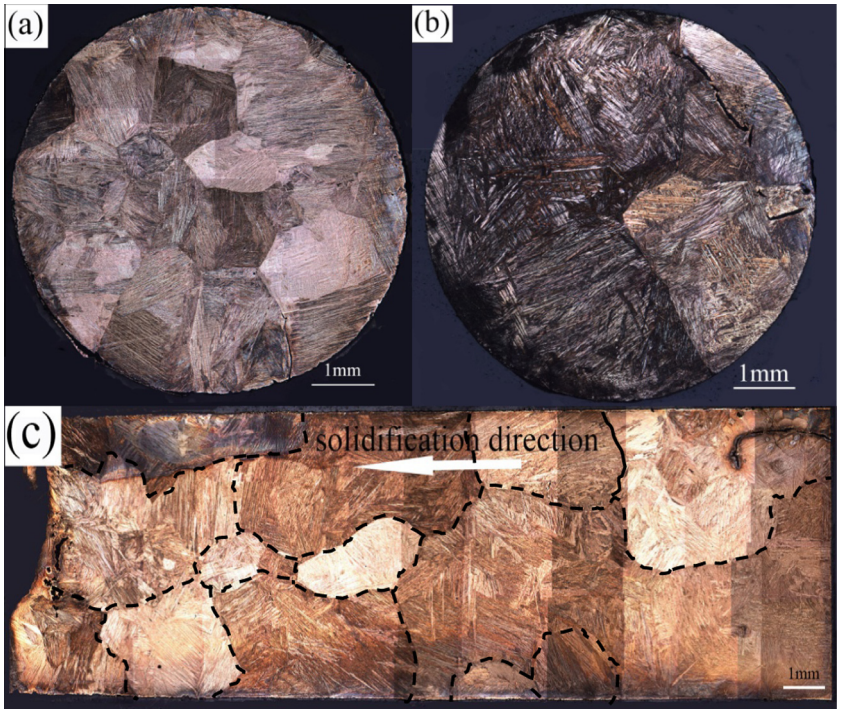

Fig. 2. Optical micrographs of polished and etched cross-sections of bulk samples fabricated by (a) non-directional furnace cooling (transverse cross-section); (b) directional solidification (transverse cross-section, perpendicular to solidification direction); and (c) directional solidification (longitudinal cross-section, parallel to solidification direction). Martensite lathes are visible within the grains.

3.2. Phase transformation behavior

All DSC curves of heat-treated samples show one distinct endothermic peak upon heating from ambient temperature, which corresponds to the martensite-to-austenite transformation, and one distinct exothermic peak on cooling which corresponds to the austenite-to-martensite transformation. The austenite start and finish temperature (A_s and A_f) are listed in Table 1 and differ significantly between bulk and porous DS samples. The A_f temperature for the DS and FC bulk samples in Table 1 is ~200 °C, which is closed to that of single crystal Cu–13.1Al–4.0Ni (wt.%) alloy [24]. By contrast, the A_f temperature of the porous samples is ~250 °C. This shift is probably due to the reduction of constraints during the martensitic transformation, but a shift in alloy composition due to processing, while unlikely, cannot be ruled out. The variation in A_f temperatures between bulk and porous samples necessitated different testing temperatures, chosen as 10 °C above A_f, i.e. 210 and 260 °C respectively.

DSC curves from the DS porous sample before and after 30 mechanical load–unload cycles are given in Fig. 4, showing that the endothermic/exothermic peaks become sharper after strain cycling, that A_s and M_s temperatures remain almost unchanged, but that A_f is reduced from ~260 to ~230 °C. It is apparent that the DS porous sample shows stable martensite transformation after mechanical cycling at high temperature.

3.3. Mechanical and superelastic properties

3.3.1. Bulk samples

A schematic stress–strain curve is given in Fig. 5a, illustrating how various mechanical parameters were determined: Young's modulus E, stress-induced martensite stress σ_{SIM}, yield stress σ_y, elastic unloading strain ε_{unload}, superelasticity-induced recovery strain ε_{se}, and residual plastic strain ε_{pl}. Fig. 5b shows, for the FC bulk sample, the stress–strain curves for eight successive load–unload compressive cycles carried out at 210 °C for increasing total strains. The strain recovered on unloading ($\varepsilon_{unload} + \varepsilon_{se}$) and the recovery ratio, defined as the ratio of this recovery strain ($\varepsilon_{unload} + \varepsilon_{se}$) to the total strain ($\varepsilon_{unload} + \varepsilon_{se} + \varepsilon_{pl}$), are listed for each cycle within Fig. 5b; it can be seen that the sample shows almost

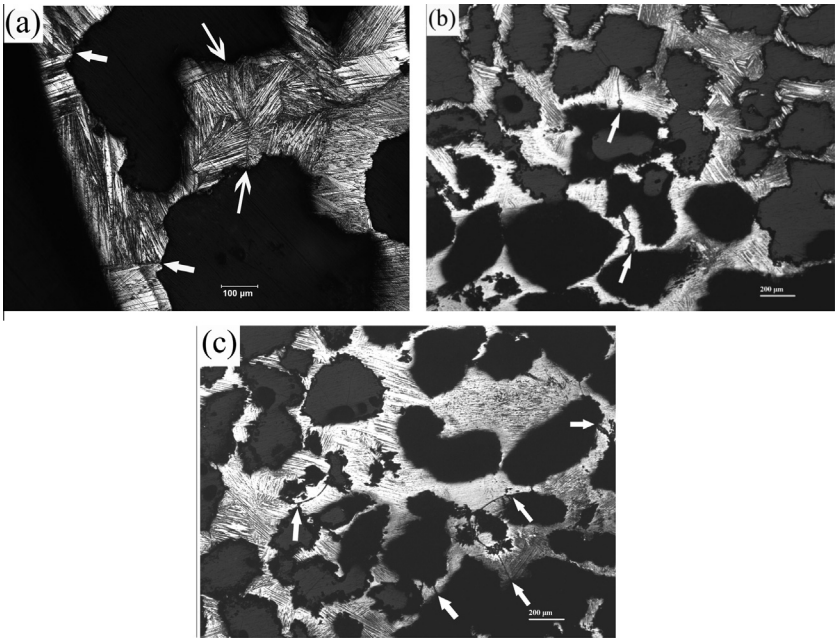

Fig. 3. Optical micrographs of polished and etched cross-sections of foams fabricated by (a) non-directional furnace cooling; directional solidification in transverse (b) and longitudinal (c) cross-section. (White coarse arrows denote grain boundaries separating bamboo grains, and a white fine arrow shows a triple point.).

Table 1
Transformation temperatures for heat-treated samples (all experiments performed on two separate samples).

Solidification	Porosity	A_f (°C)	A_s (°C)	M_s (°C)	M_f (°C)
Furnace cooled (FC)	Dense	203 ± 15	19 ± 12	159 ± 5	106 ± 3
	Porous	245 ± 4	167 ± 49	[a]	[a]
Directionally Solidified (DS)	Dense	178 ± 2	16 ± 1	146 ± 1	100 ± 1
	Porous	263 ± 4	19 ± 5	212 ± 2	18 ± 6

[a] No measured peak.

complete strain recovery for the first three cycles when the maximum applied strain is below 3%, as illustrated for the third cycle in Fig. 5c. For that cycle, the critical stress for inducing the martensitic transformation (σ_{SIM}) is ~270 MPa, beyond which the stress increases much more slowly with strain than in the previous elastic region, as expected for deformation by stress-induced martensite (SIM). The total applied strain is ~3.1% most of which is recovered on unloading (recovery ratio of 98.3%). The yield stress (σ_y) and austenite stiffness are 404 MPa and 21 GPa, respectively, Fig. 5b. For subsequent cycles where the applied strain is above 3%, the recovery ratio decreases rapidly, but the recoverable strain remains in the range 2.4–3.4 %, Fig. 5b.

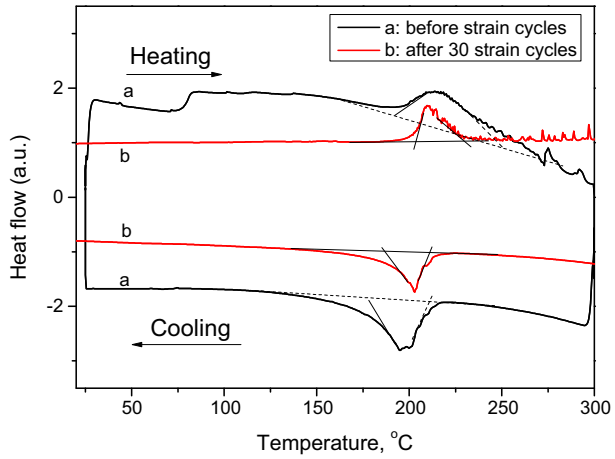

Fig. 4. DSC curves for DS foam: (a) as heat-treated sample; (b) after 30 mechanical load–unload cycles.

Fig. 6a shows the compressive mechanical cycling curves of the DS bulk sample tested at 210 °C. The sample exhibit better superelastic performance than the FC bulk sample (Fig. 5b), and near complete strain recovery when the total strain is below 6.6% (as shown by the first six cycles in Fig. 6a); σ_{SIM} is ~220 MPa, which is lower than for the FC bulk sample (270 MPa, Fig. 5a). Furthermore, a more distinct SIM plateau is present, similar in shape and amplitude to superelastic NiTi shape-memory alloy (showing 8% elastic/superelastic strain recovery) [15]. The highest nearly fully recoverable strain of 6.6% (94% recovery ratio for the sixth cycle shown in Fig. 6b) is twice that of the FC bulk sample (for the third cycle shown in Fig. 5c) and is, to our knowledge, the highest value reported in polycrystalline Cu-based SMAs at high temperature (above 100 °C) [15]. The yield stress σ_y of the DS sample is higher than that of the FC sample (660 vs. 404 MPa), while the austenite stiffnesses are similar (17 vs. 21 GPa).

The first expected effect of directional solidification is the creation of crystallographic texture which may result in reduced mismatch between neighboring grains during stress-induced transformation and thus improved superelasticity. The second effect is a size effect, as grains in DS samples are larger than in the FC samples, and in fact approach the sample smallest dimensions. Comparing the sample diameter and height (6 and 12 mm, respectively) to the grain sizes of the FC and DS bulk samples (1–1.5 and 4–5 mm, respectively), the FC samples can be considered to be polycrystalline and the DS samples to be oligocrystalline, which is similar to the bamboo-grained Cu–Zn–Al microwire in Ref. [25]. All the grains of the oligocrystalline DS bulk samples intersect the surface of the sample, whereas, for the FC bulk samples, most grains are fully surrounded by neighbors. Thus, the DS bulk sample may also owe its improved superelasticity to the reduction of intergranular incompatibility strains during stress-induced transformation as most grains intersect a free surface.

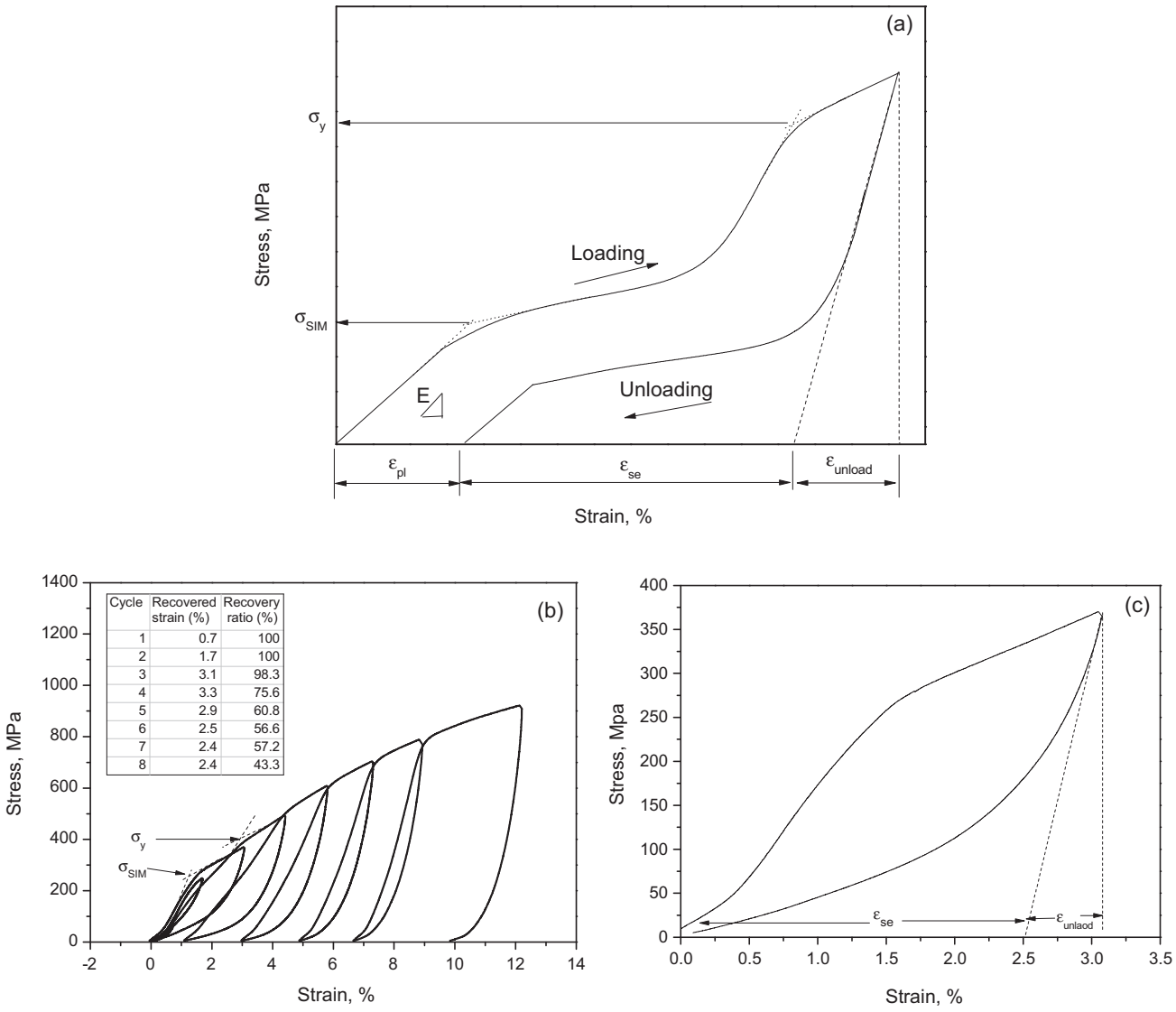

Fig. 5. Compressive stress–strain curves of FC bulk sample during load–unload cycles: (a) schematic of stress–strain curve, showing mechanical parameters; (b) all curves during 8 mechanical cycles performed to increasingly higher maximum strains at 210 °C; (c) 3rd cycle to 3% strain at 210 °C.

Here, the FC bulk sample shows ~3.1% complete strain recovery at 210 °C, which is similar to the maximal recoverable tensile strain of ~3% reported in polycrystalline Cu–14Al–3Ni (wt.%) alloys at −51 °C, but higher than the 1% value measured for this alloy at 203 °C [26]. It is generally accepted that the superelastic strain is limited by the stress/strain mismatch between neighboring grains, especially at triple junctions, during martensitic transformation, which induces cracks in the samples [27]. By contrast, the DS bulk sample exhibits 6.6% strain recovery at 210 °C, which is twice the value for the FC sample, and is lower than, but a significant fraction of, the 17% tensile strain reported for Cu–14Al–4.2Ni (wt.%) single crystals at 205 °C [15], and similar to the compressive strain recovery strain of ~7% reported in a polycrystalline superelastic NiTi alloy near ambient temperature [18]. Additionally, this compressive 6.6% strain recovery strain is higher than tensile values of 6% at 50 °C in oligocrystalline Cu–Zn–Al superelastic microwires [25], and almost the same as the tensile value of 6.8% at 50 °C in polycrystalline Cu–Al–Ni microwires [20]. It is noteworthy that the present Cu–Al–Ni polycrystalline sample was tested at 210 °C, which is higher than other literature Cu–Al–Ni SMAs reports, and usually causes instabilities in the transformation behavior due to phase precipitation. In addition to superelasticity, the stiffness of the FC bulk sample is consistent with that measured for monocrystalline Cu–Al–Ni alloys (~17–18 GPa [15]). The onset of stress-induced transformation, σ_{SIM}, is lower for the DS bulk sample than for the FC samples, as expected if the stress-induced transformation is made easier by the reduction of internal constraints. However, the yield stress of the DS bulk sample is higher than that of the FC bulk sample, which may be due to a grain texture that inhibits martensite variants formation and has a greater resolved shear stress factor [26]. A full texture analysis, which is beyond the scope of this paper, would be needed to test this hypothesis.

3.3.2. Porous samples

The three compressive mechanical cycling curves of the FC porous samples tested at 260 °C are displayed in Fig. 7a. The porous sample recovers completely in the first cycle (applied strain of 0.85%) but some residual plastic strain ε_{pl} is accumulated already in the second cycle (applied strain of 1.64%), which is plotted separately in Fig. 7b. The SIM stress (σ_{SIM} = 38 MPa) is difficult to assess, because the slope of the elastic line in the austenitic phase is almost equal to that of the SIM plateau, and it appears that some plasticity accumulates during the stiff SIM plateau, indicating that

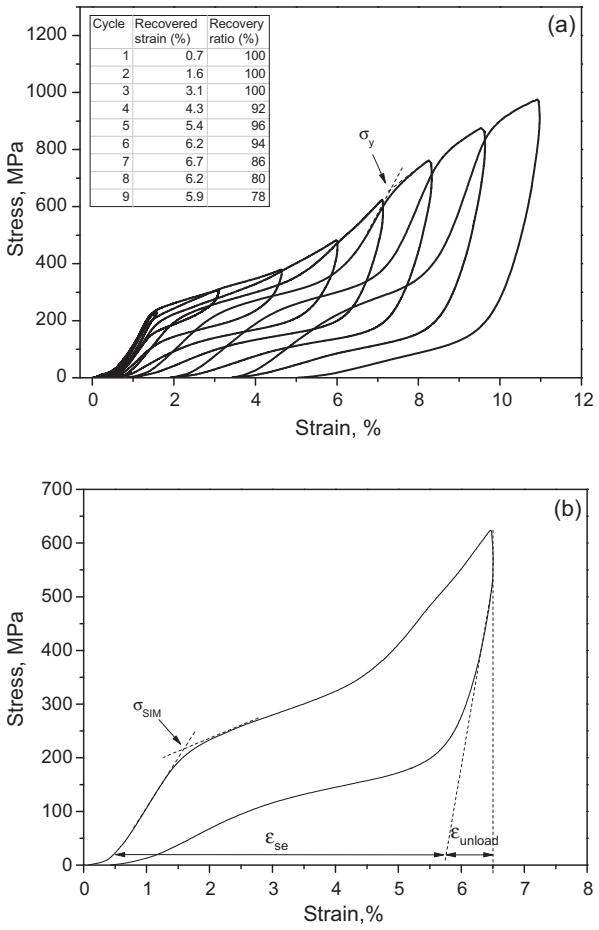

Fig. 6. Compressive stress–strain curves of DS bulk sample during mechanical cycling to increasingly higher strains at 210 °C: (a) all cycles; (b) 6th cycle.

some regions of the porous sample are plastically yielding. The stiffness calculated from the curve is about 4.2 GPa. In the third cycle (Fig. 7a), plasticity is visible as a sharply defined yield stress (σ_y = ~70 MPa), and only 69.5% of the total applied strain of 2.3% is recovered.

Fig. 8a shows the compressive mechanical cycling curves at 260 °C of the DS porous samples. This porous sample exhibits complete strain recovery up to the second cycle, with a total strain of 1.9%. For the third cycle with a total strain of 2.9% (Fig. 8b), the maximum strain recovery is 2.6%, corresponding to a recovery ratio of 89%. The DS porous sample exhibits a more defined SIM plateau than for the FC porous sample in Fig. 7b, with a value of σ_{SIM} = 36 MPa, as shown in Fig. 8b; a slight knee in the elastic range at 17 MPa may indicate small amounts of plasticity, e.g. in regions with high stress concentrations such as wall roots connecting at nodes. Both austenite stiffness (~3 GPa) and the SIM stress for the DS porous sample (Fig. 8b) are similar to values for the FC one (Fig. 7b).

The FC porous sample exhibits a maximum strain recovery strain of ~1.4%, whereas the DS one shows ~2.6% at the same testing temperature (260 °C). Furthermore, the recovery ratio for the DS porous sample still reaches values as high as 72% when the total strain is 4.66%, while a similar recovery ratio is attained at a lower strain of 2.33% in the FC one. This improvement in superelasticity for the DS porous sample is attributed to its large grain size (4–5 mm) as compared to the size of the walls separating the pores, which results in a bamboo grain structure, as shown in Fig. 3b. The strain from the martensitic transformation can thus be more easily released at the free surfaces provided by the pores, reducing incompatibility stresses and strains at grain boundaries. The texture introduced by DS is also likely to play a role in the improvement in superelasticity. A recent study [28] demonstrated the effect of texture introduced via DS upon reduction of incompatibility stresses between neighboring grains in ferromagnetic shape-memory Ni–Mn–Ga foams. Preferential orientation of grains with their ⟨100⟩ direction aligned (within an angle of 5–10°) along the solidification direction of the DS Ni–Mn–Ga foam was measured, and this texture was correlated to a two-fold improvement in magnetic-field induced strain, which is easily inhibited by incompatibility strains between grains, as compared to an untextured, furnace-cooled Ni–Mn–Ga foam. It is thus likely that texture was created by directional solidification in the present Cu–Al–Ni porous SMA, and contributed to their improvement in superelasticity.

The DS porous samples with a high porosity of 58% exhibit a 2.6% complete strain recovery at high temperature (260 °C). This result is comparable to that in Cu–Zn–Al samples with 60% porosity, which show 2.3% strain recovery at 22 °C [5]. The other mechanical properties for these Cu–Zn–Al samples (σ_{SIM} = 10 MPa and E = 2 GPa) are also similar to those of the present Cu–Ni–Al porous SMAs.

The load–unload cycling stability of superelastic alloys is important for practical applications. To study the evolution of the strain recovery in the DS porous sample, 30 load–unload cycles were performed at a constant nominal total strain of 2.7% (corresponding to a stress of ~40 MPa) at 260 °C, as shown in Fig. 9a.

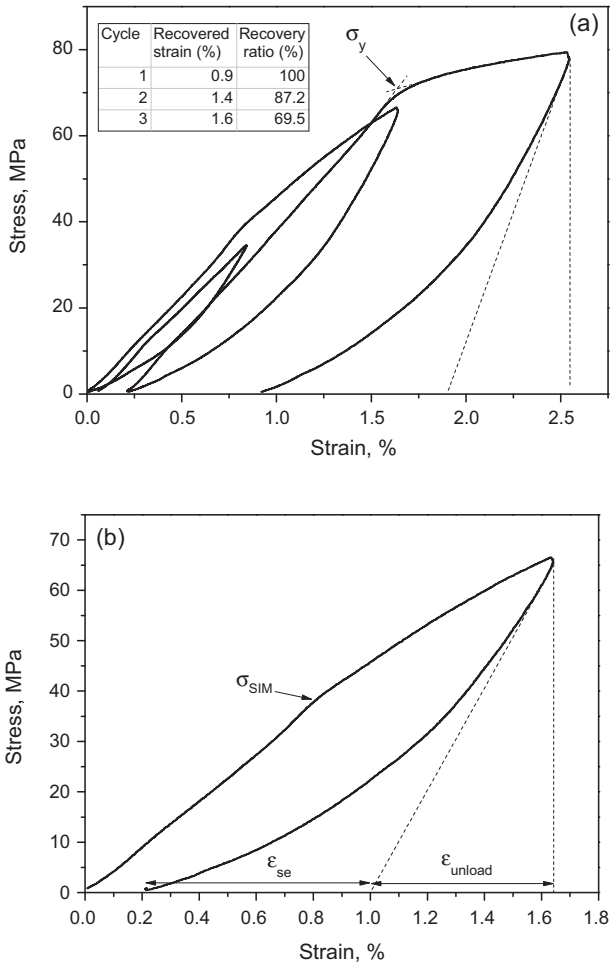

Fig. 7. Compressive stress–strain curves of FC foam during mechanical cycling to increasingly higher strains at 260 °C: (a) all cycles; (b) second cycle.

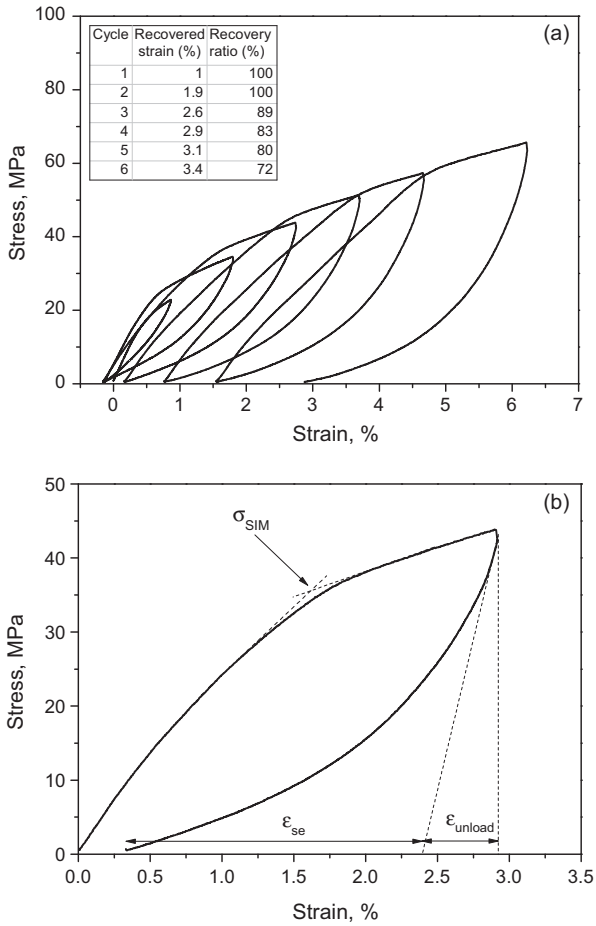

Fig. 8. Compressive stress–strain curves of DS foam during mechanical cycling to increasingly higher strains at 260 °C: (a) all cycles; (b) third cycle.

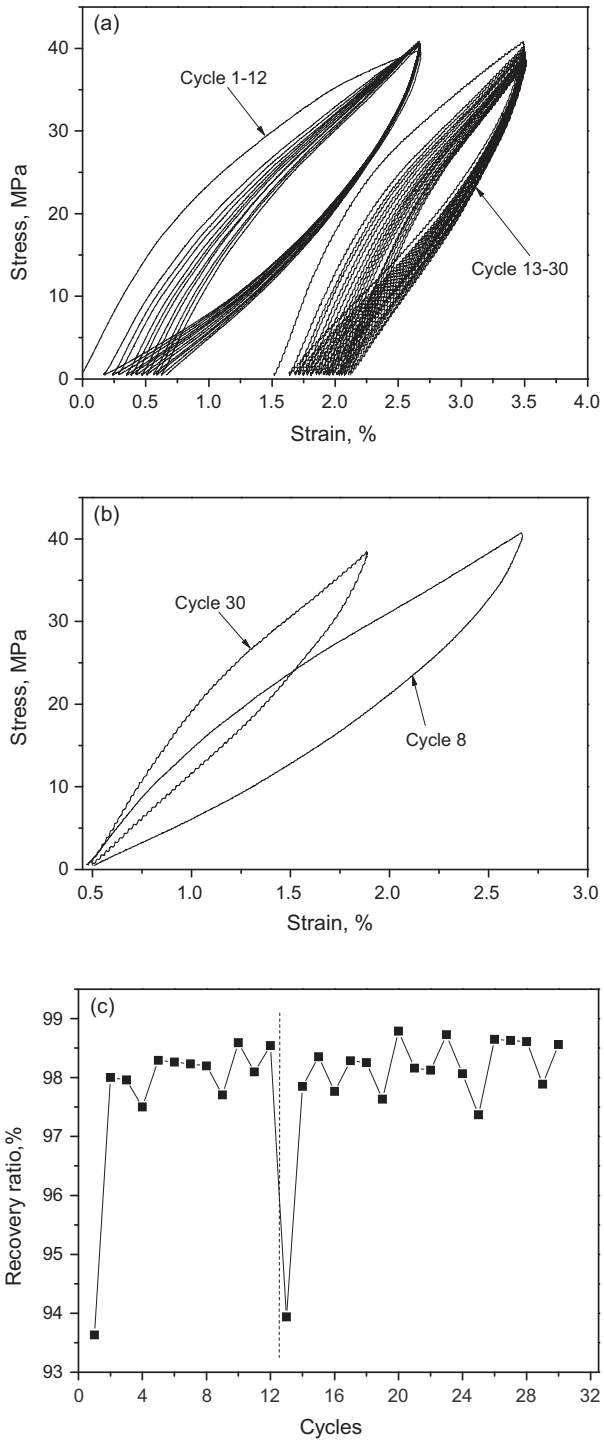

Fig. 9. Mechanical cycling of DS foam performed to a constant nominal total strain of 2.7% (corresponding to a stress of ~40 MPa) at 260 °C (a) compressive stress–strain curves for 30 cycles. The curves of cycle 13–30 are shifted to 1.5% strain to improve readability, and because the testing for cycle 13–30 was performed after an interruption of several hours (without temperature change); (b) Compressive stress–strain curves for 8th and 30th cycles; (c) plot of recovery ratio vs. cycle number.

To improve readability, the stress–strain curves for cycles 13–30 are shifted by 1.5% on the strain axis, corresponding to an interruption of several hours, without temperature change, between cycles 12 and 13. Fig. 9a shows that some plastic deformation accumulates for the first cycle of both series (cycles 1 and 13, due to "shake down"), but that residual plastic deformation becomes thereafter very small (cycles 2–12 and 14–30), with recovery ratios of 98–99% (Fig. 9c). Mechanical cycling however affects the shape of the load–unload curves: in particular, the austenite stiffness gradually increases with cycling so that the strain to achieve the maximum stress of 40 MPa decreases, together with the hysteresis on unloading. This is illustrated in Fig. 9b which shows the stress–strain curves for cycles 8 and 30. This evolution might be due to dislocations and non-transforming martensite accumulating during mechanical cycling [27]; plastic deformation is expected in regions of stress concentration within the porous structure, with the plastically deformed region becoming stabilized and unable to transform under stress. This phenomenon also appears in dense NiTi SMAs [27].

The near complete strain recovery upon unloading of each of the 30 cycles (except for the first and 13th cycle) and the general shape of the stress–strain curves in Fig. 9b indicate that repeatable and reversible stress-induced transformation can be achieved in these porous samples for at least (and probably well beyond) 30 cycles. This is confirmed by the DSC results in Fig. 4 showing that, after 30 cycles, the endothermic and exothermic peaks due to transformation appear during heating and cooling at nearly the same temperatures as in the uncycled DS porous samples. The transformation peaks are sharper for the cycled porous sample, in agreement with the superelastic training effect often observed in SMA materials, resulting from the higher mobility of martensite/austenite interfaces after multiple transformations [11].

4. Conclusions

This study investigates two methods to mitigate strain incompatibilities between grains undergoing stress-induced transformation, which reduce ductility and superelasticity in Cu–Al–Ni shape-memory alloys. The first approach, directional solidification, increases the grain size, making the sample oligocrystalline so that most grains intersect the sample surface where mismatch strains can be more easily relieved; directional solidification may also induce solidification texture, possibly reducing mismatch between neighboring grains undergoing phase transformation. The other approach introduces pores within the alloy, so that a bamboo grain structure is achieved, which reduces intergranular mismatch during transformation as a result of the free surfaces. Effect of these two methods upon the compressive superelastic properties of the alloys were tested, and the following conclusions are drawn:

- Bulk and porous directionally-solidified samples exhibit large, elongated grains, $\sim 2 \times 2 \times 6$ mm in size, approaching the sample diameter, and both show higher superelastic strain recovery as compared to control samples with smaller equiaxed grains ($\sim 1 \times 1 \times 1$ mm), which were furnace-cooled in a non-directional manner.
- The directionally-solidified, bulk sample exhibits superelastic strain recovery as high as 6.6% at 210 °C, twice the value shown by a bulk, furnace-cooled sample. Both texture and oligocrystalline grain structure may contribute to this improvement.
- The directionally-solidified porous sample shows 2.6% superelastic strain recovery at 260 °C, which is twice the value measured for the control furnace-cooled one. The enhancement is assigned to the reduction of mismatch strains among grains with bamboo structure. Also, the directionally-solidified one shows stable, repeatable strain recovery during 30 load–unload cycles at 260 °C.

Acknowledgements

This project was funded by the Army Research Office – United States (Grant 5710002979//W911NF-07-D-004-0004) through the Institute for Soldier Nanotechnologies at the Massachusetts Institute of Technology (MIT). The authors thank Prof. C.A. Schuh (MIT) for numerous useful discussions. BY also acknowledges the support of New Century Excellent Talents in University (NCET-12-0201), Guangdong Province Natural Science Fund (S2013010012487) and the Fundamental Research Funds for the Central Universities (2014ZG0026), China.

References

[1] B. Yuan, C.Y. Chung, M. Zhu, Microstructure and martensitic transformation behavior of porous NiTi shape memory alloy prepared by hot isostatic pressing processing, Mater. Sci. Eng.: A-Struct. 382 (2004) 181–187.
[2] G. Bertolino, P.A. Larochette, E.M. Castrodeza, C. Mapelli, A. Baruj, H.E. Troiani, Mechanical properties of martensitic Cu–Zn–Al foams in the pseudoelastic regime, Mater. Lett. 64 (2010) 1448–1450.
[3] T.A. Schaedler, A.J. Jacobsen, A. Torrents, A.E. Sorensen, J. Lian, J.R. Greer, et al., Ultralight metallic microlattices, Science 334 (2011) 962–965.
[4] L.J. Gibson, M.F. Ashby, Cellular Solids, Structure and Properties, Cambridge University Press, Cambridge, 1997.
[5] G. Bertolino, A. Gruttadauria, P.A. Larochette, E.M. Castrodeza, A. Baruj, H.E. Troiani, Cyclic pseudoelastic behavior and energy dissipation in as-cast Cu–Zn–Al foams of different densities, Intermetallics 19 (2011) 577–585.
[6] V.I. Itin, V.E. Gyunter, S.A. Shabalovskaya, R.L.C. Sachdeva, Mechanical-properties and shape-memory of porous nitinol, Mater. Charact. 32 (1994) 179–187.
[7] Y. Yu, L. Gu, X.Y. Lang, C.B. Zhu, T. Fujita, M.W. Chen, et al., Li storage in 3D nanoporous Au-supported nanocrystalline Tin, Adv. Mater. 23 (2011) 2443–2450.
[8] M.A. Qidwai, P.B. Entchev, D.C. Lagoudas, V.G. DeGiorgi, Modeling of the thermomechanical behavior of porous shape memory alloys, Int. J. Solids Struct. 38 (2001) 8653–8671.
[9] A. Bansiddhi, T.D. Sargeant, S.I. Stupp, D.C. Dunand, Porous NiTi for bone implants: a review, Acta Biomater. 4 (2008) 773–782.
[10] M.H. Elahinia, M. Hashemi, M. Tabesh, S.B. Bhaduri, Manufacturing and processing of NiTi implants: a review, Prog. Mater Sci. 57 (2012) 911–946.
[11] C.E. Wen, J.Y. Xiong, Y.C. Li, P.D. Hodgson, Porous shape memory alloy scaffolds for biomedical applications: a review, Phys. Scripta T139 (2010).
[12] A. Bansiddhi, D.C. Dunand, in: P.A. Netti (Ed.), Titanium and NiTi Foams for Replacing Bone in Biomedical foam for Tissue Engineering Applications, Woodhead Publishing, 2014.
[13] Y.Y. Zhao, T. Fung, L.P. Zhang, F.L. Zhang, Lost carbonate sintering process for manufacturing metal foams, Scripta Mater. 52 (2005) 295–298.
[14] T. Tadaki, Cu-based shape memory alloys, in: K. Otsuka, C. Wayman, (Eds.), Shape-memory material, Cambridge University Press, Cambridge, 1998.
[15] K. Otsuka, H. Sakamoto, K. Shimizu, Successive stress-induced martensitic transformations and associated transformation pseudoelasticity in Cu–Al–Ni alloys, Acta Metall. Mater. 27 (1979) 585–601.
[16] J. Font, J. Muntasell, J. Pons, E. Cesari, Thermal cycling effects in high temperature Cu–Al–Ni–Mn–B shape memory alloys, J. Mater. Res. 12 (1997) 2288–2297.
[17] Y. Gao, M. Zhu, J.K. Lai, Microstructure characterization and effect of thermal cycling and ageing on vanadium-doped Cu–Al–Ni–Mn high-temperature shape memory alloy, J. Mater. Sci. 33 (1998) 3579–3584.
[18] C. Greiner, S.M. Oppenheimer, D.C. Dunand, High strength, low stiffness, porous NiTi with superelastic properties, Acta Biomater. 1 (2005) 705–716.
[19] M.A. Morris, High-temperature properties of ductile Cu–Al–Ni shape memory alloys with boron additions, Acta Metall. Mater. 40 (1992) 1573–1586.
[20] Y. Chen, X.X. Zhang, D.C. Dunand, C.A. Schuh, Shape memory and superelasticity in polycrystalline Cu–Al–Ni microwires, Appl. Phys. Lett. 95 (2009).
[21] M. Chmielus, X.X. Zhang, C. Witherspoon, D.C. Dunand, P. Mullner, Giant magnetic-field-induced strains in polycrystalline Ni–Mn–Ga foams, Nat. Mater. 8 (2009) 863–866.
[22] Y. Boonyongmaneerat, M. Chmielus, D.C. Dunand, P. Mullner, Increasing magnetoplasticity in polycrystalline Ni–Mn–Ga by reducing internal constraints through porosity, Phys. Rev. Lett. 99 (2007).
[23] C. Witherspoon, P.Q. Zheng, M. Chmielus, S.C. Vogel, D.C. Dunand, P. Mullner, Texture and training of magnetic shape memory foam, Acta Mater. 61 (2013) 2113–2120.
[24] G.K. Kannarpady, A. Bhattacharyya, Cyclic isothermal stress-induced transformations in high temperature Cu–13.1Al–4.0Ni (wt.%) shape memory alloy single crystal wires, Mater. Sci. Eng.: A-Struct. 438 (2006) 719–722.
[25] S.M. Ueland, C.A. Schuh, Superelasticity and fatigue in oligocrystalline shape memory alloy microwires, Acta Mater. 60 (2012) 282–292.
[26] H. Sehitoglu, X.Y. Zhang, Y.I. Chumlyakov, I. Karaman, K. Gall, H.J. Maier, Observations on stress-induced transformations in NITI alloys, Solid Mech. Appl. 101 (2002) 103–109.
[27] J. Ma, I. Karaman, R.D. Noebe, High temperature shape memory alloys, Int. Mater. Rev. 55 (2010) 257–315.
[28] P. Zheng, N.J. Kucza, Z.L. Wang, P. Müllner, D.C. Dunand, Effect of directional solidification on texture and magnetic-field-induced strain in Ni–Mn–Ga foams with coarse grains, Acta Mater. 86 (2015) 95–101.